Tuning the aspect ratio of hydrothermally grown ZnO by choice of precursor

N. Rajeswari Yogamalar, Arumugam Chandra Bose *

Nanomaterials Laboratory, Department of Physics, National Institute of Technology, Tiruchirappalli-620 015, India

A R T I C L E   I N F O

A B S T R A C T

Variable aspect ratio (length/diameter), one dimensional ZnO nanostructures are synthesized by reacting Zn^{2+} precursor derived from $Zn \cdot Ac_2$, $Zn \cdot Cl_2$ and $Zn \cdot (NO_3)_2$ under hydrothermal treatment. The growth mechanism illustrating the formation of self-assembling from individual ZnO nanoparticles to rod-like form is explained briefly. XRD reveals that the ZnO obtained from various zinc salts are pure, wurtzite structure, with crystalline hexagonal phase. The qualitative analysis of ZnO formation and morphology of ZnO nanoparticles are estimated from FESEM and TEM micrographs. Strong UV absorption corresponding to the recombination of electron–hole pair is observed and the blue shift absorption obeys the size confinement effect. The extent of absorption relatively varies when the morphology is changed from nano-bundles to individual rod-like ZnO. When electrons are excited at wavelength of 240 nm, a strong near band edge (NBE) emission and surface defects emission are observed in the PL spectra. The broader emission situated in the blue-green region of the visible spectrum, originating from surface oxygen defects, is not observed in ZnO derived from $Zn \cdot Ac_2$.

© 2010 Elsevier Inc. All rights reserved.

1. Introduction

One dimensional transition metal oxide nanostructures [1–3] (rods, fibers, tubes, wires, ribbons) are of special interest due to their unique catalytic, electronic, optical, thermal and photonic properties intrinsically associated with their low dimensionality and the quantum size confinement effect. Among these materials ZnO has been recognized as one of the most important oxides in view of its numerous applications. ZnO nanomaterials [4,5] are a subject of intense research as low cost, efficient and environmentally friendly semiconductor materials with large band gap of 3.37 eV [6], exciton binding energy of 60 meV [7] and having a wide application in gas sensing, catalysis, energy storage, optoelectronic devices, UV lasing action, surface acoustic wave devices, piezoelectric transducers, blue light emitting diodes, transparent conducting oxides and many more [8–12]. With these aspects it is highly expected that one dimensional ZnO with tuned aspect ratios would be a potential candidate for exhibiting several interesting phenomenona.

Poly-ethylene glycol (PEG) directed hydrothermal synthesis [13–15] have been used for the acceleration of chemical reactions, moreover, the method is generally fast, simple and efficient. PEG 4000 is a non-ionic surfactant used in industry as detergency, formation of microemulsion for tertiary oil recovery and so on [16,17]. Nowadays, several reports have been appeared which explain the predictable nature of hydrothermal interactions

with reactant during the synthesis of materials. However, the exact growth mechanism still remains unclear and speculative. Many literatures have reported the controlled synthesis of one dimensional ZnO nanostructures assisted by PEG using an individual precursor and reviewed their impact on the growth, morphology and material properties in the temperature range of 70–90 °C [18–22]. In this article, we approached a simple study on the relationship, between the reaction conditions with Zn^{2+} ions derived from different precursor and their morphologies obtained at a higher temperature of 160 °C. By this contribution, the choice of precursor and morphology dependent optical properties of as-synthesized ZnO nanostructures is explored systematically.

In this paper we report on the choice of a suitable precursor for defining one dimensional ZnO nanostructures. PEG-directed hydrothermal chemical method is utilized to synthesize ZnO nanostructures from various zinc sources. The advantages of the above process are its simplicity, the low reaction temperature and their easy preparation. The growth mechanism for the hydrothermally synthesized ZnO nanostructures with the different morphology have been discussed briefly and their characterization studies including powder X-ray diffraction (XRD), field emission scanning electron microscopy (FESEM), energy dispersive X-ray fluorescence (EDX), transmission electron microscopy (TEM), Fourier transform infrared spectroscopy (FT-IR), ultraviolet visible spectroscopy (UV–vis) and photoluminescence spectroscopy (PL) are presented orderly. Further the study investigates the effect of Zn^{2+} ions derived from various zinc sources on the formation ZnO nanostructures with tunable aspect ratio. The hydrothermally synthesized ZnO nanostructures drawn from zinc acetate ($Zn \cdot Ac_2$), zinc chloride ($Zn \cdot Cl_2$) and zinc nitrate ($Zn \cdot (NO_3)_2$)

* Corresponding author. Fax: +91 431 2500133.
E-mail address: acbose@nitt.edu (A. Chandra Bose).

plays a dominant role in designing and enhancing the material properties.

2. Experimental procedures

2.1. Materials

The following reagents zinc acetate dihydrate $Zn(CH_3COO)_2 \cdot 2H_2O$, zinc chloride tetrahydrate $ZnCl_2 \cdot 4H_2O$, zinc nitrate hexahydrate $Zn(NO_3)_2 \cdot 6H_2O$, poly-ethylene glycol (PEG, Mw=4000) and ammonia (NH_3) solution are purchased from MERCK, Qualigens with 98% purity and are used without any purification. PEG act as a non-ionic surfactant mainly to limit the particle growth and to define a particular morphology.

2.2. Synthesis procedure

A surfactant solution 0.1% of PEG 4000 is prepared by dissolving in double distilled water at ambient temperature under vigorous stirring for 30 min and an appropriate amount of aqueous ammonia is added. The desired quantity of $Zn \cdot Ac_2$ precursor is dissolved in distilled water and the resulting clear solution of the metal salt is added to the surfactant solution under continuous stirring for another 30 min. The obtained white precipitate is transferred into teflon lined stainless steel autoclave and is subjected to hydrothermal heating at 160 °C for 12 h. The solid products are then centrifuged, washed with sufficient amount of distilled water and ethanol, and finally dried at room temperature. The influence and the role of precursor in defining the morphology and enhancing the physical properties of ZnO are better understood by synthesizing two more sample products with different precursors namely $Zn \cdot Cl_2$ and $Zn \cdot (NO_3)_2$ under the same synthesis condition. The sample products are named as Z1, Z2 and Z3 according to the ZnO derived from $Zn \cdot Ac_2$, $Zn \cdot Cl_2$ and $Zn \cdot (NO_3)_2$ precursor, respectively.

## 3. Results and discussion

3.1. Crystal structure and phase analysis

The powder X-ray diffraction study is performed with Rigaku Ultima III diffractometer using Cu $K_{\alpha1}$ radiation of wavelength 1.5406 Å. A beam voltage of 45 kV and a 40 mA beam current are used. The data is collected in the 2θ range of 20–80° with a continuous scan rate of 0.2°/min and the phase is identified by using joint committee on powder diffraction standard (JCPDS) database. The structure and phase purity of all the samples are investigated by powder XRD. Fig. 1a shows the XRD patterns of as-synthesized ZnO nanostructures from varying zinc source and indexed according to the standard ZnO pattern (JCPDS Card ID 36-1451). The standard XRD pattern of ZnO and their miller indices are used for relative comparison. The as-synthesized ZnO nanopowders produced diffraction pattern with large number of peaks and all are well indexed as crystalline hexagonal phase wurtzite structure. The d-spacing values and unit cell parameters 'a' and 'c' obtained from XRD data for all the ZnO samples are matched with the standard JCPDS files of bulk ZnO and are tabulated in Table 1. The average crystalline size of the as-prepared ZnO samples are determined using the Debye–Scherrer formula (Eq. (1)) with the integral widths corrected with standard Si sample (Eq. (2)) using Cauchy–Lorentzian fit [23]. For crystalline size analysis, the high intense (1 0 1) reflection of the hexagonal phase ZnO is employed:

$$R = 0.9\lambda/\beta\cos\theta \tag{1}$$
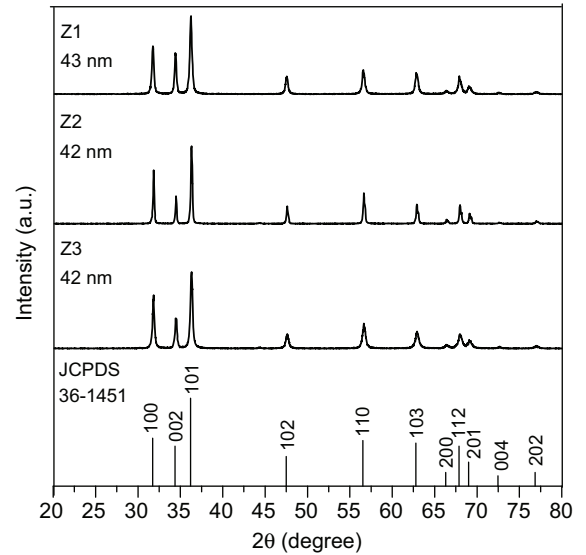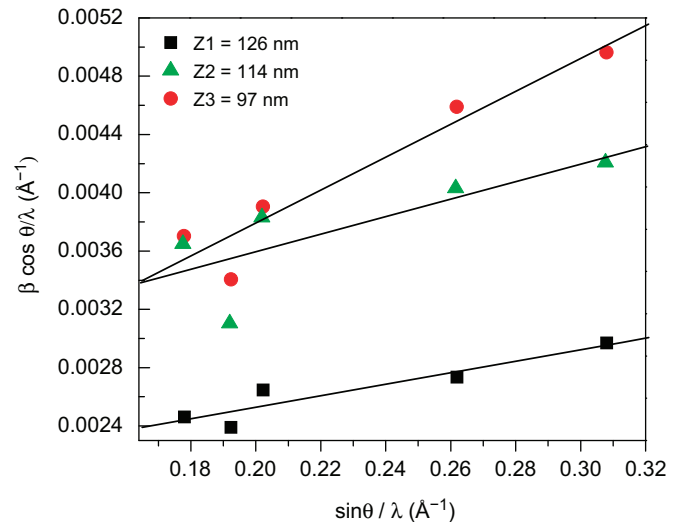
Fig. 1. (a) Indexed XRD patterns of PEG-directed hydrothermal synthesized ZnO nanostructures along with the standard XRD pattern of ZnO. (b) Crystallite size and strain estimation from WH plot.

where R is the average crystallite size, λ the Cu $K_{\alpha1}$ radiation of wavelength 1.5406 Å, β is the full width at half maximum in radians and θ the scattering angle in degree. The corrected instrumental broadening for Lorentzian fit is given by

$$\beta = \beta_{measured} - \beta_{instrumental} \tag{2}$$

Williamson Hall (WH) X-ray line broadening analysis provides a method of finding an average size of coherently diffracting domains and strain. WH plot is drawn for high intense XRD peaks and their crystallite size and strain are deconvoluted using the equation

$$\frac{\beta\cos\theta}{\lambda} = \frac{k}{R} + \varepsilon\frac{\sin\theta}{\lambda} \tag{3}$$

where k is a constant and its value is 0.9, ε is the lattice strain, λ the Cu $K_{\alpha1}$ radiation of wavelength 1.5406 Å, β the full width at half maximum and θ the scattering angle. The intercept of the plot between $\beta\cos\theta/\lambda$ and $\sin\theta/\lambda$ shown in Fig. 1b gives the inverse of particle size (R) and the slope of the curve determines the strain (ε) associated with the lattice dislocation. The particle size and strain

values of as-synthesized ZnO nanostructures Z1, Z2 and Z3 estimated from WH analysis are also tabulated in Table 1.
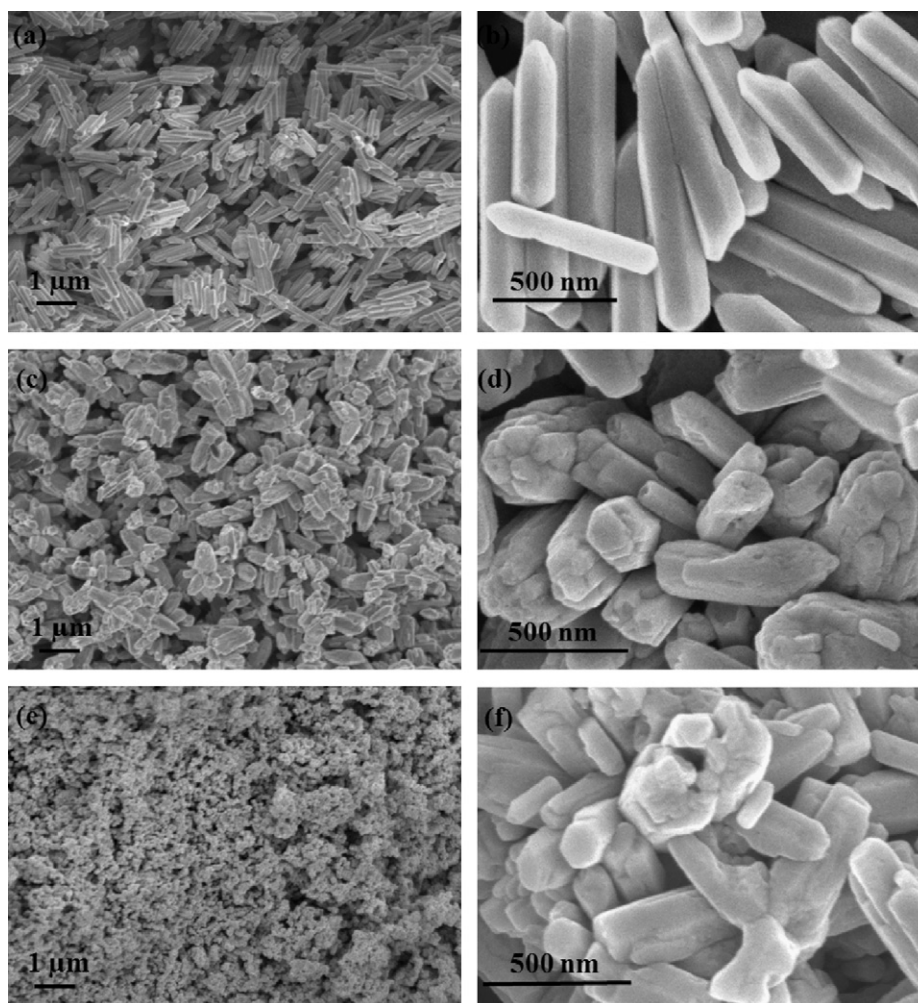
3.2. ZnO nanostructures

The morphology of the as-prepared products are examined by FESEM equipped with EDX on Hitachi S4800 Instrument with an accelerating voltage of 3 kV and a beam current of 1 mA. Fig. 2a–f displays the SEM micrographs of ZnO nanostructures obtained from $Zn \cdot Ac_2$, $Zn \cdot Cl_2$ and $Zn \cdot (NO_3)_2$, respectively. In Fig. 2a one can see the ZnO nanorods indexed as Z1 exhibits a wide size distribution. The length of the rods is in micron range (650–1100 nm) and the diameter runs from 150 to 200 nm. On the whole the average length and diameter of the nanorods are estimated to be 771 and 178 nm, respectively. The average aspect ratio (length/diameter) of

Z1 is calculated to be 4.33. Most of these nanorods have regular hexagonal shaped rod-like structure, highly dispersed with one end closed and the other, having a blunt tip.

Particles are found as agglomerates in the case of ZnO nanoparticles (Z2) synthesized from $Zn \cdot Cl_2$ zinc source (shown in Fig. 2c, d). Bundles of ZnO nanoparticles are observed at low and high magnified SEM images. Here, four to six short ZnO nanorods are grouped to form a single bundle. The bundle comprises of ZnO nanorods with varying length and diameter. Few rods are found to be separated and oriented randomly. One end of the rod is hexagonal in shape. The formation of nano-bundles with short rods indicates that the nucleation is rapid while, the particle growth is highly inhibited. Because of the above explanation, the crystallite size of ZnO (Z2) is smaller and the emission intensity observed in PL spectra (discussed later) is more intense than Z1.

Table 1
XRD measurements of as-synthesized ZnO nanostructures.

S. no.	Sample	Scherrer method (nm)	WH analysis (nm)	β (radians)	d-spacing (Å)	Strain ε (no unit)	Cell volume, V (Å)^3	Lattice parameter		
								a (Å)	c (Å)	c/a
1	Z1	43	126	0.004570	2.4715	0.00271	47.461	3.2475	5.1966	1.6002
2	Z2	42	114	0.004622	2.4715	0.00274	47.423	3.2461	5.1968	1.6009
3	Z3	42	97	0.004762	2.4717	0.00147	47.431	3.2462	5.1973	1.6010

Fig. 2. FESEM images of ZnO nanostructures (a, b) derived from $Zn \cdot Ac_2$ (Z1) with an aspect ratio of 4.50, (c, d) flakes of agglomerates Z2 resulted from $Zn.Cl_2$ source and (e, f) ZnO nanorods Z3 obtained from $Zn(NO_3)_2$ precursor.

No definite size and shape of the particles can be described from SEM micrographs as they are highly aggregated in nature. Fig. 2e, f shows the FESEM images of ZnO nanorods derived from $Zn \cdot (NO_3)_2$ precursor (Z3). The length and diameter of the rods are comparatively smaller, shorter than those rods fabricated from $Zn \cdot Ac_2$ (Z1) and $Zn \cdot Cl_2$ (Z2). The formation of Z3 nanorods is more or less similar to that of Z2 and thus, they exhibit an analogous growth mechanism. The elemental composition and the presence of zinc and oxygen of the as-synthesized ZnO nanostructures (Z1, Z2 and Z3) are confirmed from EDX measurements. Fig. 3a–c is the EDX plot of ZnO nanostructures derived from various zinc sources. The atomic and weight percentage of zinc and oxygen are determined from EDX. It is observed that the Zn/O ratio in Z1, Z2 and Z3 are 1.30, 1.43 and 1.45 respectively.

Morphology, individual particle size and crystallinity of the sample products were examined by TEM, and SAED measurements using JEOL JEM FX II equipment. The TEM and SAED pattern provides a detailed study on the microstructure and growth direction of ZnO nanostructures. TEM micrographs of as-prepared ZnO nanostructures derived from various precursors are shown in Fig. 4a–f and their corresponding SAED patterns are shown as an inset in the figure. The entire SAED pattern indicates that the ZnO nanostructures Z1, Z2 and Z3 are single crystalline with [0 0 1] growth direction. Here, the ZnO belongs to wurtzite hexagonal structure with space group $P6_3mc$ in which the O^{2-} and Zn^{2+} ions are alternatively coordinated along the c-axis [24]. The TEM images of ZnO designated as Z1 shown in Fig. 4a, b is composed of straight nanorods with smooth surface and blunt end. The measured aspect ratio is found to be around 4.5. Fig. 4c, d and e, f is the TEM micrographs of ZnO derived from $Zn \cdot Cl_2$ and $Zn \cdot (NO_3)_2$ precursors, respectively. In contrast to ZnO derived from $Zn \cdot Ac_2$, the Z2 and Z3 consist of highly short and irregular nanorods of varying length and diameter. As the particle growth is highly inhibited, the surface-volume ratio is increased with increased surface activation energy thereby bringing the particle closer and binding them together to form a bundle of indefinite shape and size as seen from their SEM images (Ref. Fig. 2c, d). When $Zn \cdot (NO_3)_2$ is used instead of $Zn \cdot Cl_2$ the general shape of the particles are preserved but their aspect ratio changed due to the lower height of the hexagonal rod. The TEM also confirms that the ends of Z2 and Z3 nanorods are hexagonal in nature and their aspect ratios are 3.20 and 2.30, respectively. SEM, TEM and SAED analysis demonstrated that the choice of precursor could have a significant influence on the growth of ZnO nanostructures and hence provide a useful route for the morphologies of ZnO nanostructures.
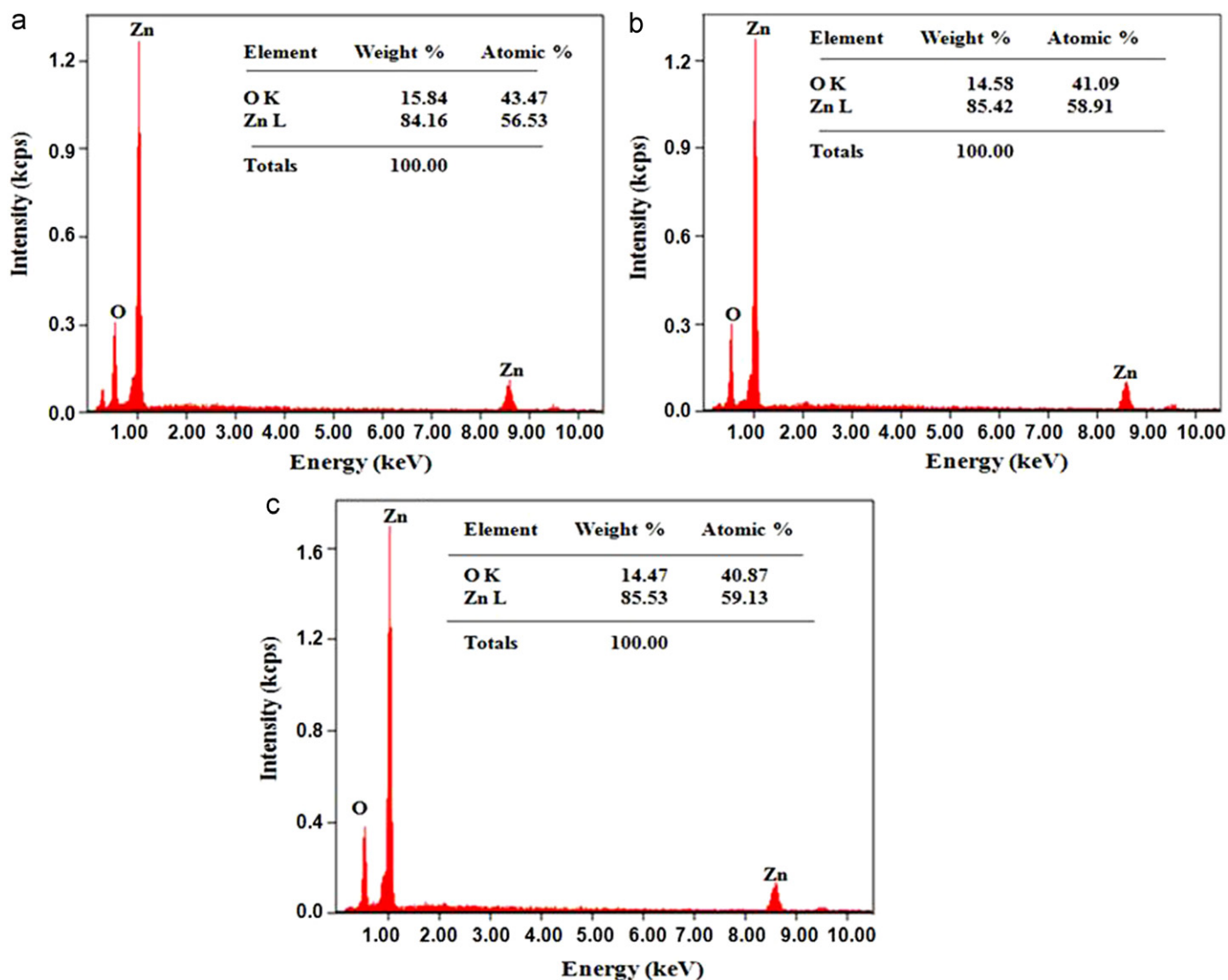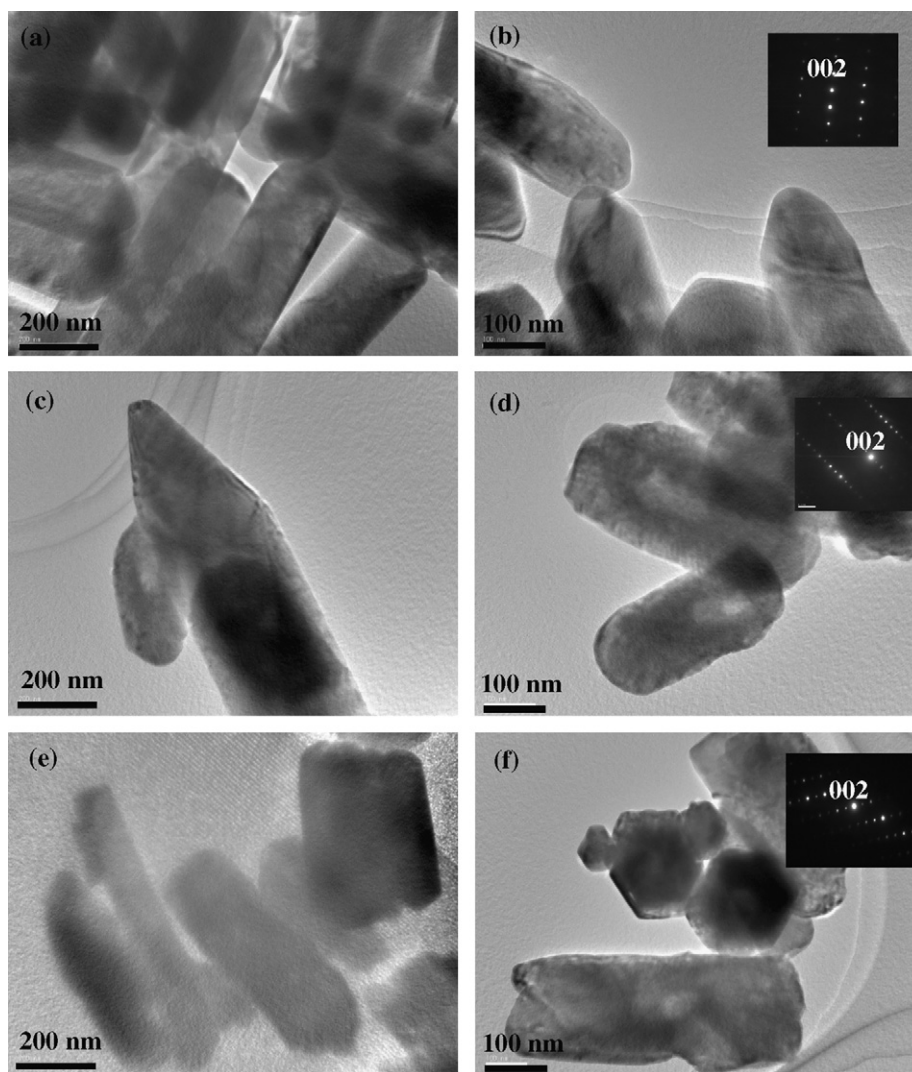

Fig. 3. The EDX plot of (a) Z1, (b) Z2 and (c) Z3 and their chemical composition are mentioned as an inset.
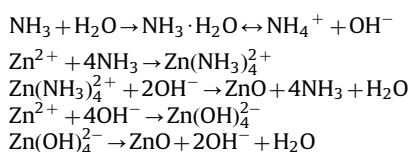
Fig. 4. TEM micrographs and the corresponding SAED pattern (shown as an inset) of ZnO nanostructures (a, b) derived from $Zn \cdot Ac_2$ (sample Z1) with an aspect ratio of 4.50, (c, d) flakes of agglomerates Z2 resulted from $Zn \cdot Cl_2$ source and (e, f) ZnO nanorods Z3 obtained from $Zn(NO_3)_2$ precursor.

3.3. Morphology evolution

Changing the nature of the zinc salt in the experimental condition affects the uniformity, distribution of the particles and the shape of the ZnO particles. The mechanism and formation of ZnO nanorods and nanorod aggregations are schematically represented in Fig. 5. Two prime factors can be reasoned out for the effect of the zinc source on the formation of ZnO crystals.

In our experimental work, the growth of ZnO nanostructures is mainly affected by the temperature and pH of the sample solution. In all the three samples, a constant temperature of 160 °C is assigned and pH of the solution is adjusted to 7–8 by controlled addition of ammonia solution. In the presence of ammonia, the mechanism for the formation of ZnO nanostructures is usually accepted as follows [25]:

$$NH_3 + H_2O \rightarrow NH_3 \cdot H_2O \leftrightarrow NH_4^+ + OH^-$$

$$Zn^{2+} + 4NH_3 \rightarrow Zn(NH_3)_4^{2+}$$
$$Zn(NH_3)_4^{2+} + 2OH^- \rightarrow ZnO + 4NH_3 + H_2O$$
$$Zn^{2+} + 4OH^- \rightarrow Zn(OH)_4^{2-}$$
$$Zn(OH)_4^{2-} \rightarrow ZnO + 2OH^- + H_2O$$

From the above equations it is very clear that ZnO nuclei are formed by the dehydration of $Zn(NH_3)_4^{2+}$ or $Zn(OH)_4^{2-}$. The effective reason for the precursor affecting the morphology of ZnO could
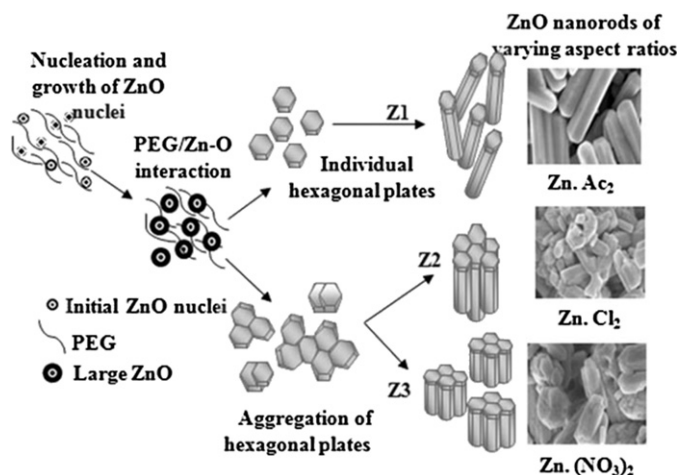
Fig. 5. Schematic representation of ZnO nanorods and nano-bundles formation under PEG directed hydrothermal synthesis.

be attributed to different reaction pathways, solubility of the precursor, and basicity of the solution which influenced the crystal nucleation and growth [26–30]. In the hydrothermal process when

the concentration of Zn^{2+} and OH^- reached the super-saturation degree of ZnO, ZnO nuclei would form according to the above chemical reaction. The nuclei originating from Z2 and Z3 experience low basicity as their intermediate by product are strong acid such as HCl and HNO_3 acid in contrast to the weak acetic acid formed in the case of Z1. The reaction speed of the sample with low basicity (Z2 and Z3) is increased tremendously thus producing multiples of ZnO nuclei within a short interval. As the reaction speed is increased part of the crystal would dissolve into the solution thus, a well defined monodispersed rod-like structure is not favorable at this condition. The above explanation clearly suggests that the reaction pathways, basicity and solubility of the solution influence the crystal nucleation and growth.

The second reason can be explained on the balance exhibited between the nucleation rate and growth rate of the particle. When the growth rate dominates over the nucleation rate, the crystallite size increases, while in the case of nucleation domination the crystallite size decreases. In addition, the nature of the anions CH_3COO^-, NO_3^- and Cl^- present in the reaction decides the degree of aggregation and re-arrangement of primary particles. Here, comes the role of PEG in assembling and modifying the morphology of ZnO nanostructures. Poly-ethylene glycol $(H(OCH_2CH_2)_nOH)$ is a non-ionic surfactant with $-O-$ as hydrophilic and $-CH_2-CH_2-$ as hydrophobic end. The non-ionic hydrophilic end associated with water is the ether oxygen's of PEG. In each case, the hydrophilic end of the surfactant is strongly attracted to the water molecules, since the force of attraction between hydrophobic group and water is less. As a result the surfactant molecules self-assemble at the surface and internally so that the hydrophile end is towards the water molecule and the hydropobe end is squeezed away from the water. At this stage the long chain molecule is converted into ring pattern. Now, under hydrothermal condition, the growth units $Zn(NH_3)_4^{2+}$ or $Zn(OH)_4^{2-}$ is easily absorbed by the atom O in C–O–C chain, so that they can be carried and transformed into ZnO crystalline particles and grow on active sites around the surface of ZnO nuclei. Based on the degree of adsorption, the electrostatic force of attraction and interaction between the PEG molecules and Zn^{2+} ionic group a particular morphology with specific orientation is synthesized. Compared with acetate ion, the divalent nitrate and chloride ion are smaller in size and they can be easily encapsulated by long chain PEG molecule. The capping induced by PEG confines the growth of the Z2 and Z3 nanoparticles and thus, prevents the re-arrangement of primary particles in preferred direction.

3.4. Functional group analysis

Fig. 6 shows the presence of characteristic functional groups in as-prepared ZnO nanorods recorded by FT-IR, using a Perkin Elmer FT-IR spectrophotometer in the range 400–4000 cm^{-1}. For all the as-prepared ZnO nanorods there are functional groups among 1050–1150 cm^{-1} which were assigned to the stretching of ether groups. The characteristic absorption of alkyl (R-CH_2) stretching modes (between 2850 and 3000 cm^{-1}) and also the peaks between 1490 and 1300 cm^{-1} suggests the absorption of PEG molecule on the surface of ZnO nanoparticles [31]. The broad peaks observed at 3000–3600 cm^{-1} are due to hydrated water and peaks at 1600–1640 cm^{-1} are due to the presence of some overtones. The peaks at 550 and 450 cm^{-1} corresponds to the metal–oxygen vibrational modes of ZnO compounds having a sharp and high intense peak [32,33]. FT-IR bands at 533, 498 and 418 cm^{-1} are observed for aggregated ZnO nanorods derived from $Zn \cdot Cl_2$ and $Zn \cdot (NO_3)_2$ precursor as shown separately in Fig. 6b. No sharp splitting of IR band is observed in the case of highly oriented ZnO nanorods synthesized from $Zn \cdot Ac_2$. The superposition of two or three separate bands to form a single broad band and their

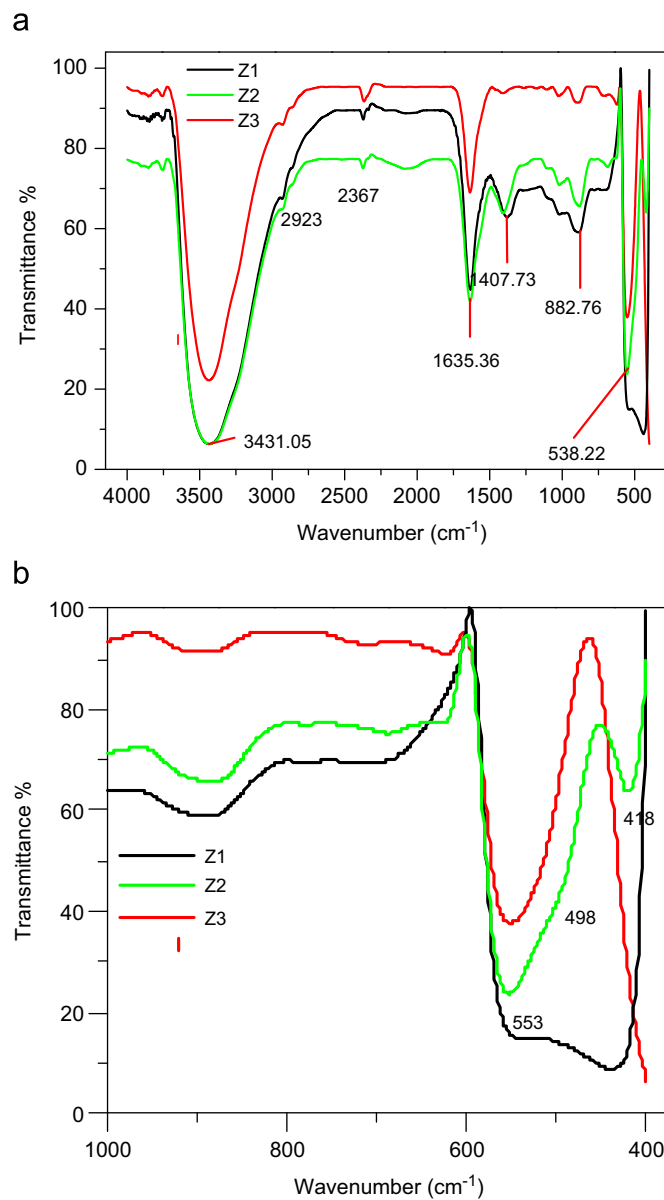**Fig. 6.** (a) FT-IR spectra of ZnO nanostructres obtained from $Zn \cdot Ac_2$ (Z1), $Zn \cdot Cl_2$ (Z2) and $Zn \cdot (NO_3)_2$ (Z3), respectively and (b) the extended view in the wavelength range 400–1000 cm^{-1}.

existence in IR spectrum of ZnO particles expresses the choice of precursor for defining particular morphology with preferred orientation [34].

3.5. Optical studies

Room temperature optical spectra in the UV and visible light wavelength ranges are recorded using Shimadzu UV-1700 Pharma spectrophotometer. Fig. 7a shows the UV–vis absorption spectra of ZnO nanostructures obtained with different Zn^{2+} precursors revealing a significant difference. The onset of absorption is obtained by extrapolating the steep part of the rising absorption curve. The maximum absorption peak of ZnO derived from $Zn \cdot Ac_2$, $Zn \cdot Cl_2$ and $Zn \cdot (NO_3)_2$ appeared at 374, 372 and 370 nm, respectively, which exhibits a slight red shift relative to bulk hexagonal ZnO phase (369 nm). In principal, the absorption coefficient at the photon energy below the optical band gap termed as tail

absorption depends exponentially on the photon energy. The relation is given by

$$\alpha(h\nu) \sim \exp\left(\frac{h\nu}{E_u}\right) \qquad (4)$$

where E_u is the Urbach's energy and is calculated from the inverse slope of the curve plotted between $\ln \alpha$ against $h\nu$ shown as an inset in Fig. 7a. The absorption coefficient α has been calculated from the measured absorbance A through

$$\alpha = \frac{2.303\rho 10^6}{lCM} A \qquad (5)$$

where ρ stands for the density of ZnO, M the molecular weight, C the molar concentration of ZnO and l is the optical path length. The Urbach's energy measures the standard of crystal disorder and electronic band structure [35,36]. The calculated values of Urbach's energy are listed in Table 2 and their values increases in the order of

$Z1 < Z2 < Z3$. Thus, E_u the optical parameter elucidate that the one dimensional ZnO nanostructure derived from zinc acetate are more ordered than Z2 and Z3. Considering a direct band gap transition for ZnO, the optical band gap of ZnO nanostructures are estimated from the linear fit in plot of $(\alpha h\nu)^2$ against the energy $h\nu$ in eV, as shown in Fig. 7b. The nanostructures synthesized from $Zn \cdot Ac_2$ solution exhibit optical band gap of 2.93 eV, whereas those from $Zn \cdot Cl_2$ and $Zn \cdot (NO_3)_2$ precursor show optical band gap of 2.97 and 2.99 eV, respectively. The variation of optical band gap energy and the lattice parameter 'a' as a function of crystallite size are plotted in Fig. 7c. The plot clearly depicts that the optical band gap energy decreases with increase in particle size, as the energy are inversely proportional to the square of crystal radius.
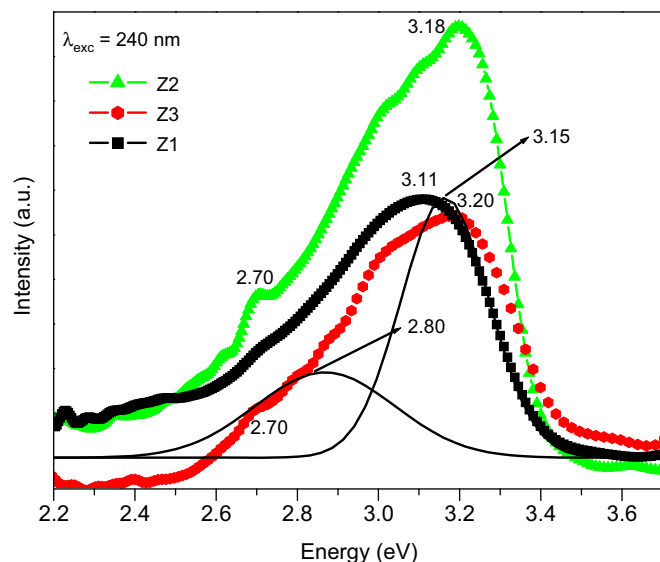
Fig. 8 shows the room temperature PL emission spectrum measured at 240 nm wavelength excitation using Shimadzu (RF-5301 PC) spectrofluorophotometer for ZnO synthesized from various precursors. Samples Z1, Z2 and Z3 exhibits peak around UV region (3.10–3.20 eV) which can be attributed to the NBE emission
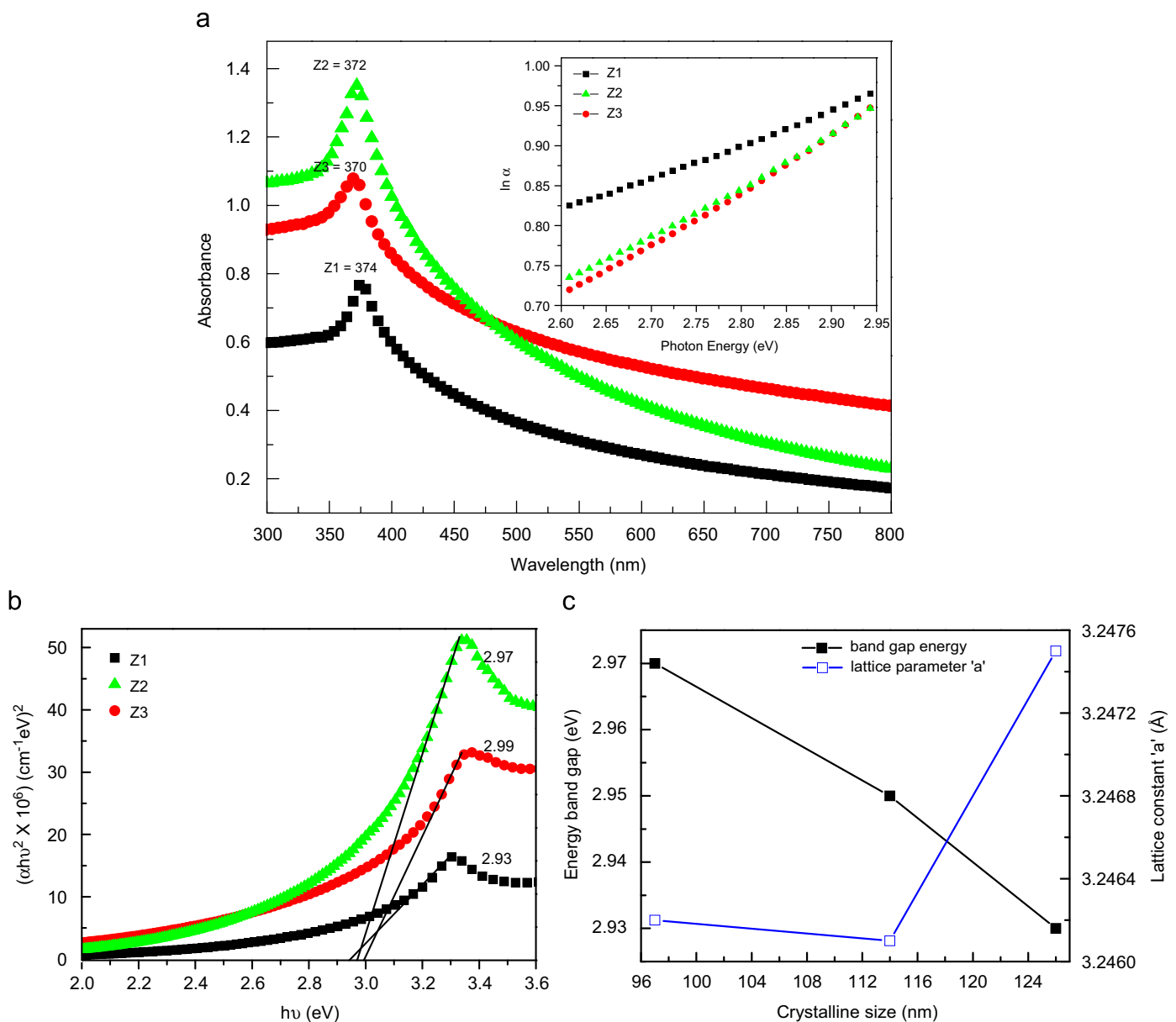
Fig. 7. (a) The absorption spectra of the ZnO products prepared at 160 °C for 12 h using different zinc source. The inset shows a plot of $\ln \alpha$ versus photon energy E (eV). (b) Plot of $(\alpha h\nu)^2$ against the energy $h\nu$ in eV for ZnO nanostructures derived from varying source. (c) Variation of lattice parameter 'a' and energy band gap E_g (eV) with the particle size estimated from WH plot.

Table 2
Generalized calculations in the synthesis of ZnO nanostructures under PEG directed hydrothermal synthesis.

Sample	WH analysis (nm)	Mean particle size (TEM) (nm)		Aspect ratio (no unit)	Optical band gap (eV)	Urbach energy (meV)	PL emission (eV)	
		Mean length	Mean diameter				NBE emission	Blue emission
Z1	126	771	178	4.50	2.93	96	3.11	–
Z2	114	401	175	3.20	2.97	178	3.18	2.70
Z3	97	400	125	2.30	2.99	181	3.20	2.70

Fig. 8. The room temperature PL emission spectrum of ZnO derived from various precursors measured at 240 nm wavelength excitation.

that comes from the free hole–electron pair transition. The NBE emission peak also decreases with increase in crystallite size as resulted from UV–vis absorbance spectrum. When the PL emission spectrum of ZnO derived from $Zn \cdot Cl_2$ (Z2) is deconvoluted using a Gaussian fit, it shows two peaks centered at 2.80 and 3.15 eV. The weak blue emission peak at 2.80 eV (443 nm) is due to various surface defects resulting from oxygen and zinc vacancies [37–39]. It is observed only for ZnO derived from $Zn \cdot Cl_2$ and $Zn \cdot (NO_3)_2$ precursor. It meant that the as-synthesized rod-like ZnO nanostructures Z2 and Z3 had high concentration of surface defects with low stoichiometric nature. This emission can be easily correlated with the similar growth mechanism exhibited by Z2 and Z3 as indicated under the head ZnO nanostructures. Thus, the ZnO synthesized from $Zn \cdot Ac_2$ are pure and defect free. Further, it can be concluded that the precursor plays not only an important role in tailoring the morphology of ZnO nanostructures but, also alter and enhance the physical properties of ZnO nanomaterials. Table 2 depicts the overall measurements performed in the synthesis of ZnO nanostructures under PEG-directed hydrothermal synthesis.

4. Conclusions

In summary, this paper concludes that the various experimental conditions including precursor/PEG concentration, hydrothermal temperature, reaction time, basicity of the solution decides the nucleation, growth and final morphology of ZnO nanostructures. The analysis of XRD patterns established the formation of wurtzite structure hexagonal phase ZnO nanostructures. TEM image of the as-synthesized ZnO with its corresponding SAED pattern exhibited

the single crystalline nature of the nanorod. The absorption of PEG on the surface of ZnO nanoparticles and the formation of ZnO are confirmed by FT-IR spectra. The illustrated growth mechanism of ZnO nanorods are in tune with the structural observations revealed from XRD, SEM and TEM images. ZnO with aggregated nanorods derived from $Zn \cdot (NO_3)_2$ yielded an aspect ratio of 2.3 lower than the ZnO nanorods obtained from $Zn \cdot Ac_2$ (4.5). Hence, the crystal morphology and the aspect ratio of nanorods can be easily tuned by varying the Zn^{2+} ions extracted from various zinc sources. The optical absorption studies revealed that the transition is direct band–band transition and the energy band gaps are determined to be in the range of 2.93–3.00 eV. The presence of surface defects and NBE emission are observed from PL spectrum.

References

[1] S.P. Antony, J.I. Lee, J.K. Kim, Appl. Phys. Lett. 90 (2007) 103107–103110.
[2] Y. Xia, P. Yang, Y. Sun, Y. Wu, B. Mayers, B. Gates, Y. Yin, F. Kim, H. Yang, Adv. Mater. 15 (2003) 353–389.
[3] J. Hu, T. Wang Odom, C.M. Lieber, Acc. Chem. Res. 32 (1999) 435–445.
[4] H. Hosono, Thin Solid Films 515 (2007) 6000–6014.
[5] Z. Fan, J.G. Lu, Int. J. High Speed Electron. Syst. 16 (2006) 883–896.
[6] J.H. Lee, K. Kamada, J. Colloid Interface Sci. 316 (2007) 887–892.
[7] Z. Ajji, Nucl. Instrum. Meth. Phys. Res. B 265 (2007) 179–182.
[8] Y.W. Heo, D.P. Norton, L.C. Tien, Y. Kwon, B.S. Kang, F. Ren, S.J. Pearton, Mater. Sci. Eng. R 47 (2004) 1–47.
[9] Y. Zhang, K. Yu, D. Jiang, Z. Zhu, H. Geng, L. Luo, Appl. Surf. Sci. 242 (2005) 212–217.
[10] J.H. Song, J. Zhou, Z.L. Wang, Nano Lett. 6 (2006) 1656–1662.
[11] B. Xiang, P. Wang, X. Zhang, A. Dayeh, P.R. Aplin, C. Soci, D. Yu, D. Wang, Nano Lett. 7 (2007) 323–328.
[12] S.J. Pearton, D.P. Norton, K. Ip, Y.W. Heo, T. Steiner, Superlattices Microstruct. 34 (2003) 3–32.
[13] X. Zhou, D. Zhang, Y. Zhu, Y. Shen, X. Guo, W. Ding, Y. Chen, J. Phys. Chem. B 110 (2006) 25734–25739.
[14] H. Yang, Y. Song, L. Li, J. Ma, D. Chen, S. Mai, H. Zhao, Cryst. Growth Des. 3 (2008) 1039–1043.
[15] S.M. Ghoreishi, H. Naeimi, M.D. Navid, Bull. Korean Chem. Soc. 26 (2005) 548–552.
[16] W. Von Rybinski, M.J. Schwuger, Nonionic Surfactants Physical Chemistry, Marcel Dekker Inc., New York, 1987.
[17] J.T.G. Overbeek, P.L. De Bruyn, F. Verhoeckx, Surfactants, Academic Press, London, 1984.
[18] T. Busgen, M. Hilgendorff, S. Irsen, F. Wilhelm, A. Rogalev, D. Goll, M. Giersig, J. Phys. Chem. C 112 (2008) 2412–2417.
[19] M. Guo, P. Diao, S. Cai, J. Sol. State Chem. 178 (2005) 1864–1873.
[20] C. Wang, E. Shen, E. Wang, L. Gao, Z. Kang, C. Tian, Y. Lan, C. Zhang, Mater. Lett. 59 (2005) 2867–2871.
[21] W. James, L. Katherine, J. Zhang, H. Kosel, M. Kuno, Chem. Mater. 16 (2004) 5260–5272.
[22] J. Zhang, L. Sun, J. Yin, H. Su, C. Liao, C. Yan, Chem. Mater. 14 (2002) 4172–4177.
[23] P. Singh, A. Kumar, A. Kaushal, D. Kaur, A. Pandey, R.N. Goyal, Bull. Mater. Sci. 31 (2008) 573–577.

[24] U. Ozgura, I. Alivov, C. Liu, A. Teke, M.A. Reshchikov, S. Dogan, V. Avrutin, S.J. Cho, H. Morkocd, J. Appl. Phys. 98 (2005) 041301-103.
[25] X. Hou, F. Zhou, B. Yu, W. Liu, Mater. Lett. 61 (2007) 2551–2555.
[26] Y. Tak, K. Yong, J. Phys. Chem. B 109 (2005) 19263–19269.
[27] S. Cho, S.H. Jung, K.H. Lee, J. Phys. Chem. C 112 (2008) 12769–12776.
[28] H.S. Qian, S.H. Yu, J.Y. Gong, L.B. Luo, L.L. Wen, Cryst. Growth Des. 5 (2005) 935–939.
[29] S. Music, D. Dragčevic, M. Maljkovic, S. Popovic, Mater. Chem. Phys. 77 (2002) 521–530.
[30] E. Arca, K. Fleischer, I.V. Shvets, J. Phys. Chem. C 113 (2009) 21074–21081.
[31] S. Liufu, H. Xiao, Y. Li, Powder Technol. 145 (2004) 20–24.
[32] Y.D. Wang, S. Zhang, C.L. Ma, H.D. Li, J. Lumin. 126 (2007) 661–664.

[33] M. Li, X. Liu, D. Cui, H. Yu, M. Jiang, Mater. Res. Bull. 41 (2006) 1259–1265.
[34] X. Qiu, L. Li, J. Zheng, J. Liu, X. Sun, G. Li, J. Phys. Chem. C 112 (2008) 12242–12248.
[35] S.K. Arora, A.J. Kothari, R.G. Patel, K.M. Chauhan, B.N. Chudasama, J. Phys. Conf. Ser 28 (2006) 48–52.
[36] S.M. Reda, Energy Res. J. 1 (2010) 36–41.
[37] D.M. Hofmann, D. Pfisterer, J. Sann, B.K. Meyer, R. Tena-Zaera, V. Munoz-sanjose, T. Frank, G. Pensl, Appl. Phys. A 88 (2007) 147–151.
[38] Y.S. Fu, X.W. Du, S.A. Kulinich, J.S. Qiu, W.J. Qin, R. Li, J. Sun, J. Liu, J. Am. Chem. Soc. 129 (2007) 16029–16033.
[39] L. Tian, S.J. Kim, H.L. Park, S. Mho, Mater. Res. Bull. 41 (2006) 29–37.